ACS Chemical Neuroscience

pubs.acs.org/chemneuro Research Article

Atrial Natriuretic Peptide Associated with Cardiovascular Diseases Inhibits Amyloid-β Aggregation via Cross-Seeding

Yijing Tang, Dong Zhang, Yung Chang, and Jie Zheng*

Cite This: ACS Chem. Neurosci. 2023, 14, 312−322 Read Online

ACCESS | Metrics & More | Article Recommendations | Supporting Information

ABSTRACT: Both cardiovascular diseases (CVDs) and Alzheimer's disease (AD) share some common risk factors (e.g., age, obesity, oxidative stress, inflammation, hypertension) that contribute to their overlapping pathogenesis, indicating a "head-to-heart" pathological connection between CVDs and AD. To explore this potential connection at the protein level, we study the potential cross-seeding (heterotypic interactions) between CVD-associated atrial natriuretic peptide (ANP) and AD-associated β-amyloid (Aβ). Collective aggregation and cell assays demonstrate the cross-seeding of ANP with different Aβ species including monomers, oligomers, and fibrils with high binding affinity (K_D = 1.234−1.797 μM) in a dose-dependent manner. Such ANP-induced cross-seeding also modifies the Aβ aggregation pathway, fibril morphology, and cell deposition pattern by inhibiting Aβ fibrillization from small aggregates, disassembling preformed Aβ fibrils, and alleviating Aβ-associated cytotoxicity. Finally, using transgenic *C. elegans* worms that express the human muscle-specific $A\beta_{1-42}$, ANP can also effectively delay Aβ-induced worm paralysis, decrease Aβ plaques in worm brains, and reduce reactive oxygen species (ROS) production, confirming its in vivo inhibition ability to prevent neurodevelopmental toxicity in worms. This work discovers not only a new cross-seeding system between the two disease-related proteins but also a new finding that ANP possesses a new biological function as an Aβ inhibitor in the nonaggregated state.

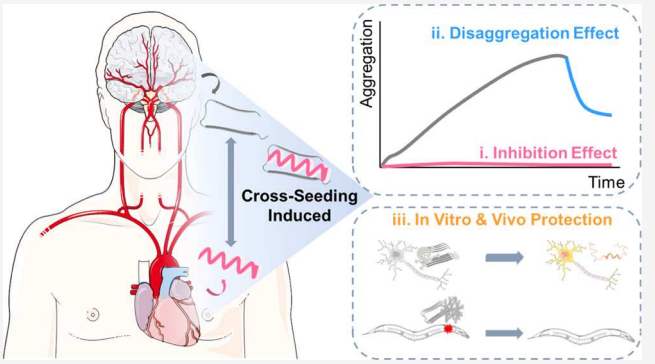

KEYWORDS: *atrial natriuretic peptide, β-amyloid, cross-seeding, cardiovascular dysfunctions, Alzheimer's disease, amyloid peptides*

1. INTRODUCTION

Alzheimer's disease (AD), as the most common age-related neurodegenerative disorder, is pathologically featured by extracellular senile plaques formed by amyloid-β (Aβ) and intracellular neurofibrillary tangles formed by the hyperphosphorylated tau protein,[1,2] which eventually cause the progressive loss of cognitive ability, memory, and language.[3] As a multifactorial and chronic disease, different genetic and nongenetic factors are reported to contribute to the pathogenesis of AD. Genetic factors include the inherited APP mutants (presenilin 1, presenilin 2), apolipoprotein E, neurotransmitters, adenosine triphosphate (ATP)-binding cassette transporter, bridging integrator protein 1, and others, while nongenetic factors (i.e., exogenous factors) includes cerebrovascular diseases, type 2 diabetes, brain trauma, microbial infection, stroke, sleep disorders, metabolic disorders, obesity, and others.[4−6] Clinical studies have shown that only less than 1% AD patients have inherited genetic deficiency, while AD in most patients (>95%) derives from the complicated interplay between multiple genetic and nongenetic factors.[7,8]

Among different genetic and nongenetic factors, cardiovascular disorders (CVDs) including atrial fibrillation, coronary artery disease, heart valve disease, and heart failure have 3−6 times higher risk of developing AD.[9] Mutually, AD is also prevalent in patients with CVDs,[10] as evidenced by the higher occurrence of ischemic microvascular lesions in the brains of AD patients.[11] Meanwhile, AD and CVD patients appear to share some common risk factors of hypertension, dyslipidemia, hypercholesterolemia, and hyperhomocysteinemia.[12−15] Some mechanisms including Aβ metabolism, tau phosphorylation, oxidative stress, microbial infection, and neuroinflammation[16−21] have also been proposed for explaining the bidirectional communication between AD and CVDs. For a typical instance, the circulation of Aβ in blood often interrupts the metabolic processes of cardiomyocytes and damages cardiac functions, which in turn worsens the symptoms of AD via amyloid overproduction, mitochondrial dysfunction, ROS accumulation, and neuroinflammation in the cerebral

Received: November 20, 2022
Accepted: December 19, 2022
Published: December 28, 2022

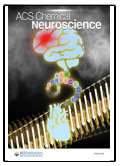

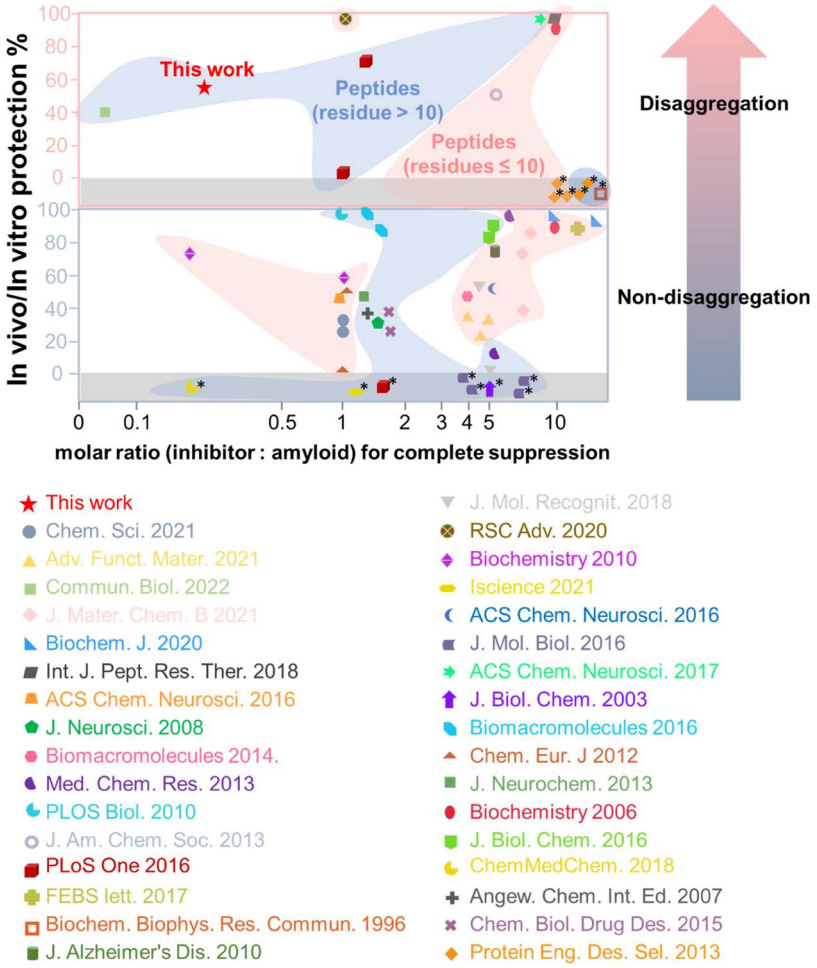

Figure 1. Summary of the inhibition performance of peptide-based Aβ inhibitors with >10 residues (blue area) and ≤10 residues (pink area) in terms of the minimal molar ratio of an inhibitor to induce complete inhibition, in vivo/in vitro protection from amyloid-induced cytotoxicity, and the capacity to disaggregate preformed amyloid fibrils. * cell/animal data are not available in the references. Table S1 also provides the inhibition performance of different peptide-based Aβ inhibitors.

region.[22−24] While the exact links and mechanisms between CVDs and AD still remain largely unknown, the heterotypic interactions between different disease-related proteins are considered as a pathological risk factor to mutually cause and promote each disease (this process is known as cross-seeding), which have been less explored with respect to the role of the heart−brain axis in the spreading mechanism between AD and CVDs.

Considering a close relationship between CVDs and AD, here, we investigated the potential cross-seeding (heterotypic interactions[25,26]) between the CVD-related atrial natriuretic peptide (ANP) and AD-related Aβ and examined whether Aβ aggregation and toxicity can be modulated by cross-seeding using in vitro and in vivo experiments. ANP with 28 residues (Figure 2), belonging to a family of endogenous hormone peptides, is predominately produced by cardiomyocytes in the central nervous system and peripheral tissues.[27] Under healthy conditions, ANP plays a central role in controlling blood pressure, diuresis, natriuresis, and the secretion of other hormones (e.g., aldosterone, vasopressin, and renin).[28] ANP is usually rapidly eliminated by neutral endopeptidase and natriuretic peptide receptor C, leading to a short $t_{1/2}$ of 2−5 min. However, under disease conditions, the increased plasma level of ANP is often associated with heart failure and hypertension, thus ANP also serves as a biomarker for the diagnosis and treatment of heart failure. More importantly, ANP tends to accumulate on the surface of atrial myocytes to form β-structure-rich, amyloid-like aggregates, i.e., isolated atrial amyloid (IAA).[29,30]Apart from similar amyloid-like structures between ANP and Aβ,[31] both ANP and Aβ are known to cause age-associated amyloidosis[32] and found to co-exist in blood circulation,[33,34] which increases the possibilities for their cross-seeding or co-aggregation with other amyloid proteins.[35]

To test the abovementioned hypothesis, we examined the potential cross-seeding between ANP and Aβ and the cross-seeding impacts on Aβ aggregation and toxicity in vitro and in vivo. Using thioflavin T (ThT) fluorescence, surface plasmon resonance (SPR) spectroscopy, atomic force microscopy (AFM), and circular dichroism (CD), we demonstrated that ANP can interact with Aβ species at different aggregation stages to induce dose-dependent inhibition of Aβ at sub-stoichiometric concentrations (≤equimolar ratio) via different inhibition pathways, i.e., (i) ANP can bind the monomeric and oligomeric Aβ species at the very early stage to modulate their structure transition and further aggregation and (ii) ANP can also disassemble the preformed Aβ fibrils and convert them into small aggregates. Cell assays confirmed that cross-seeding

https://doi.org/10.1021/acschemneuro.2c00712
ACS Chem. Neurosci. 2023, 14, 312−322

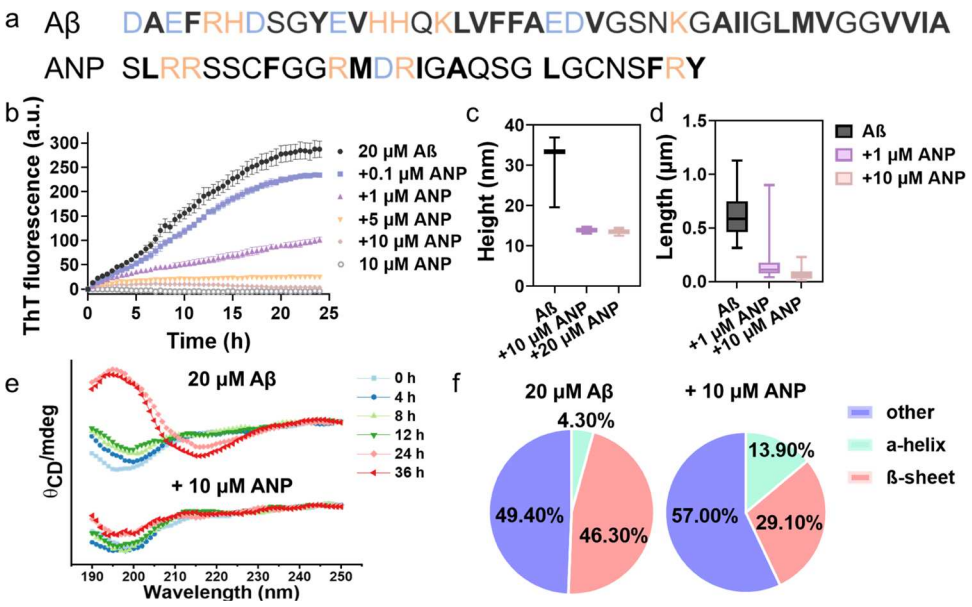

Figure 2. Cross-seeding of ANP with Aβ inhibits amyloid fibrillization. (a) Sequence characterization of Aβ and ANP. Color ID: positively charged residues (orange letters) and negatively charged residues (blue letters), hydrophobic residues (bold). (b) ThT kinetic profiles of Aβ (20 μM) aggregation in the absence and presence of ANP (0.1−10 μM) for 24 h, demonstrating that ANP prevents Aβ aggregation in a dose-dependent manner. All data represent mean ± standard error of triplicate measurements. Morphological analysis of AFM images in Figure S1 to characterize the average (c) heights and (d) lengths of cross-seeding aggregates formed by 20 μM Aβ and 10−20 μM ANP. The upper, middle, and lower bars define the max, mean, and min values of aggregate heights and lengths, respectively. (e) Time-dependent circular dichroism (CD) spectra and (f) the corresponding secondary structure distributions of pure Aβ (20 μM) and cross-seeding Aβ-ANP (20:10 μM) aggregates during 24 h aggregation.

of ANP with Aβ reduced Aβ-induced cell toxicity in vitro. Finally, we applied *Caenorhabditis elegans* and its genetic mutants as an in vivo model for evaluating the neurotoxicity of ANP-Aβ cross-seeding. *C. elegans* was selected because of several advantages including the short life cycle from egg to adult, short lifespan between 2 and 3 weeks, translucent body for easy visual assessment, and ready spreading in the nervous system due to lack of BBB. The worm results showed that ANP significantly inhibited AD-like symptoms of worm paralysis, suppressed Aβ deposits in the head region of the worms, and diminished ROS production caused by oxidative stress. From an amyloid inhibitor viewpoint in Figure 1, most of the peptide-based Aβ inhibitors[36,37] comprise short sequences with ≤10 residues, which exhibit some intrinsic disadvantages, including (i) limited inhibition efficiency (equimolar inhibitors only lead to <30% inhibition of Aβ aggregation),[38] (ii) high concentrations (inhibitor: Aβ > 6:1),[39] (iii) poor cell protection (~20−60% of cell viability),[40] or (iv) low binding affinity (K_D = 9−156 μM).[41,42] For comparison, peptide inhibitors with residues >10 are more efficient at inhibiting Aβ aggregation and toxicity, presumably due to their high enzymatic proteolysis resistance, high structural stability, and multiple reactive sites. For instance, equimolar antimicrobial peptides of defensins can inhibit 100% Aβ aggregation and thus rescue 35% of neuron cells,[43] while a very small amount of SEVI (1 μM) can completely inhibit Aβ aggregation (20 μM) and increase cell viability by 40%.[44] Our ANP outperforms other peptide inhibitors of Aβ in terms of inhibition efficiency. Due to the multifactorial nature of both proteins and protein-related diseases, nonaggregated ANP possesses a new biological function as an Aβ inhibitor, while aggregated ANP could be a causative factor for Aβ. This work provides new insights into the structure, origin, and aggregation principles of cross-seeding between the two disease-related proteins, which helps to understand the potential link between CVDs and AD.

2. RESULTS AND DISCUSSION

2.1. Cross-Seeding of ANP with Monomeric Aβ Inhibits Amyloid Aggregation. Despite a certain clinical relationship between CVD and AD, it still remains unclear (i) whether AD-related Aβ can cross-seed with CVD-related ANP to form amyloid-like aggregates with characteristic β-rich structures and (ii) if occurring, whether Aβ aggregation could be modified by heterotypic interactions (cross-seeding) between Aβ and ANP. To examine this cross-seeding scenario, thioflavin T (ThT) assay was first performed to study heterotypic interactions (cross-seeding) between Aβ (20 μM) and ANP (0−10 μM) at different Aβ/ANP ratios (1:0.005−1:0.5) at 37 °C for 24 h. As shown in Figure 2b, pure ANP of 10 μM did not produce any fluorescence signal, which not only indicates non-self-aggregation of ANP at this highest concentration but also ensures no ThT signal from ANP self-aggregation to be contributed to Aβ-ANP cross-seeding. In sharp contrast, pure Aβ of 20 μM exhibited a typical nucleation−polymerization kinetics of amyloid fibrillation, starting with a short lag phase of 0.5 h (nuclei formation), followed by a rapid growth phase of 0.5−20 h (protofibril formation), finally reaching an equilibrium phase of 20−24 h at a stable ThT plateau of ~287 au (mature fibril formation),

When co-incubating nonamylogenic ANP (0−10 μM) with Aβ (20 μM), ANP of all tested sub-stoichiometric concentrations (≤equimolar ratio) showed a dose-dependent inhibition of Aβ aggregation at all aggregation stages, as evidence by (i) the increase of lag time from 0.5 to 25 h (i.e., complete inhibition), (ii) the reduction of the aggregation rate at the growth phase, and (iii) the decrease of the final ThT

https://doi.org/10.1021/acschemneuro.2c00712
ACS Chem. Neurosci. 2023, 14, 312−322

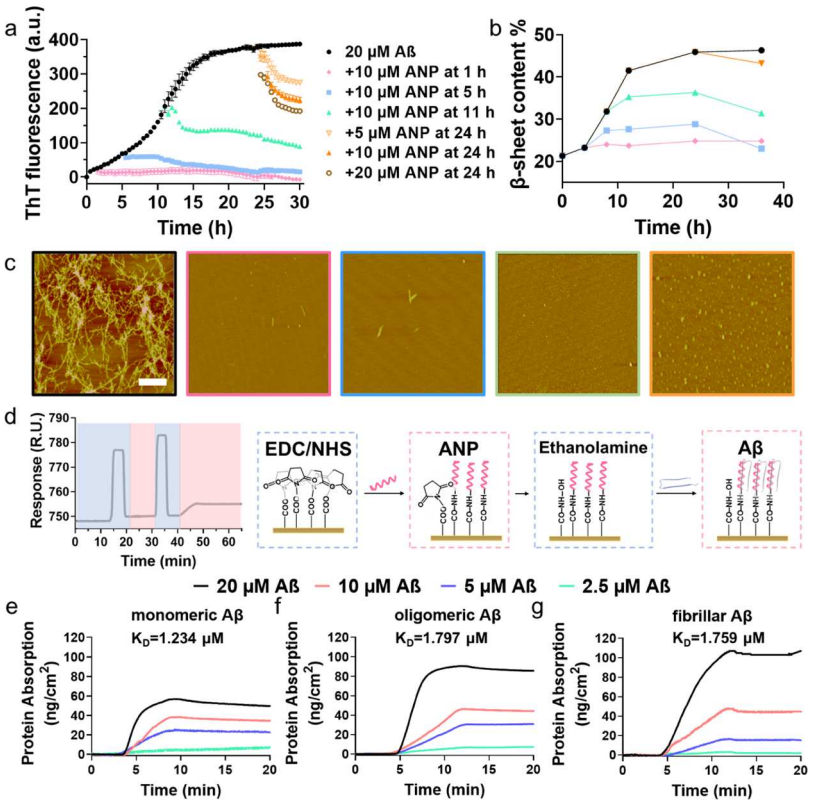

Figure 3. Inhibition of seed-induced aggregation of Aβ by ANP. (a) Time-dependent ThT fluorescence curves, (b) β-structure contents, and (c) representative AFM images after adding ANP (5−20 μM) to Aβ seeds (20 μM) preformed in the 1 h-lag phase (pink), 5 h-early-growth phase (blue), 11 h-late-growth phase (green), or 24 h-equilibrium phase (orange). (d) Schematic workflow for immobilizing ANP on the SPR chip for Aβ binding. SPR sensorgrams show the adsorption amount of (e) monomeric Aβ, (f) oligomeric Aβ, and (g) fibrillar Aβ of varied concentrations of 2.5−20 μM on the ANP-coated SPR surface.

intensity at the equilibrium phase. Quantitively, at the highest Aβ/ANP molar ratio of 1:0.5, ANP (10 μM) was able to completely suppress Aβ aggregation. Further decrease of Aβ/ANP ratios from 1:0.25 to 1:0.005 led to 91.5, 64.8, and 18.5% reduction in Aβ fibrilization, indicating a general inhibition of Aβ aggregation via ANP-Aβ cross-seeding. AFM images of these ANP-Aβ hetero-assemblies, obtained at different time points, are shown in Figure S1. As controls, pure Aβ aggregation (20 μM) underwent the morphological change and growth from a few short protofibrils with an average height/length of 15/206 nm in 5 h to long and dense fibrils with an average height/length of 33/605 nm at 24 h. However, the introduction of 1 μM ANP (the lowest concentration tested) to a freshly prepared Aβ solution (20 μM) significantly delayed the formation of mature fibrils during 24 h incubation, as indicated by the absence of large mature fibrils, but the formation of short fibrils with the average height/length of 13/173 nm. When increasing of ANP concentration to 10 μM, ANP-induced amyloid inhibition became more pronounced, leading to very few aggregates with an average height/length of 13/73 nm (Figure 2c,d).

To better understand the inhibition data from ThT and AFM, we applied CD spectroscopy to monitor the changes in the secondary structure during the entire fibrillization process of Aβ (20 μM) with and without ANP (10 μM) (Figures 2e and S2a−c). As a control, the self-aggregation of Aβ followed a typical structural transition from the random coil (as indicated by the negative peak at 198 nm) to a β-sheet-rich structure (as indicated by the negative peak at ∼215 nm and positive peak at ∼195 nm), finally leading to 49.4% random coil, 4.3% α-helix, and 46.3% β-sheet after 24 h (Figures 2f and S2d−f). For comparison, when cross-seeding of ANP with Aβ at two extreme ratios of 0.05:1 and 0.5:1, the negative peak at ∼215 nm almost disappeared, while the positive peak at ∼195 nm flattened, clearly reflecting a slow structural transition from random coils to β-structures and a decrease in the β-sheet content. Figure 2f clearly revealed that upon co-incubation of ANP with Aβ for 24 h, the random coil structure increased from 49.4 to 57%, while the β-structure decreased from 46.3 to 29.1%, as compared with pure Aβ incubation. In line with the ThT and AFM results, such a structural transition, particularly the decrease in β-sheet content, was less pronounced as the decrease in ANP concentrations, showing concentration dependence. Collectively, side-by-side comparisons of ThT, AFM, and CD data demonstrate (i) the existence of the cross-seeding between Aβ and ANP, given the nonamyloidogenic nature of ANPs of <10 μM and (ii) the cross-seeding-induced inhibition of Aβ fibrillization. Such cross-seeding-induced Aβ inhibition mainly stems from the stabilization of the random coil structure of Aβ monomers, so as to prevent or modulate their misfolding and aggregation pathways by reducing the production of β-sheet-rich structures.

2.2. Cross-Seeding of ANP with Different Aβ Seeds Modulates Amyloid Aggregation Pathways. To gain insights into the cross-seeding pathways between ANP and different Aβ species, we designed and conducted different cross-seeding experiments by adding ANP (5−20 μM) to different Aβ seeds (20 μM) preformed at different aggregation

https://doi.org/10.1021/acschemneuro.2c00712
ACS Chem. Neurosci. 2023, 14, 312−322

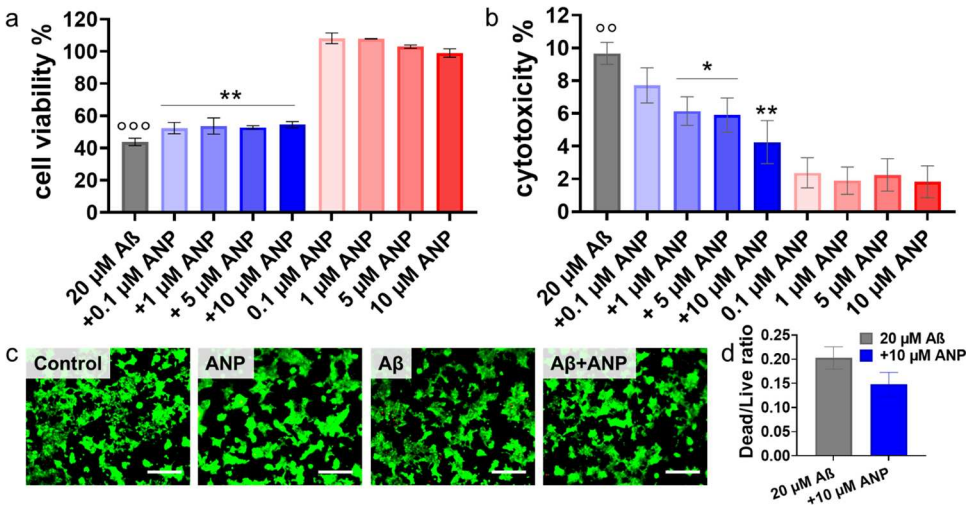

Figure 4. Cross-seeding of ANP with Aβ alleviates Aβ-associated cytotoxicity. (a) MTT assay for cell viability and (b) LDH assay for cell toxicity under the incubation of 20 μM Aβ in the presence and absence of ANP at molar ratios of 1:0.005−1:0.5. Data were normalized by the untreated cell group (positive control, 100% MTT reduction, and 0% LDH activity) and Triton X-100-treated cells (negative control, 100% LDH activity). The t-test was used for data analysis (n = 3) for cells treated with ANP or Aβ alone relative to the control ($^{\circ\circ\circ}p < 0.005$, $^{\circ\circ\circ\circ}p < 0.001$), as well as cells treated with mixed ANP-Aβ relative to cells treated with Aβ alone ($^{*}p < 0.05$; $^{**}p < 0.01$). (c) Representative fluorescence microscopy images and (d) the corresponding analysis of live/dead cell ratios for cells treated with freshly prepared Aβ (20 μM) solutions co-incubated for 24 h with and without 10 μM ANP. Untreated cells were set as a control group. Red and green fluorescence indicates dead and live cells, respectively. Scale bar = 180 μm.

stages, including 1 h-lag phase, 5 h-early growth phase, 11 h-middle of the growth phase, and 24 h-equilibrium phase. In this way, we were able to (i) determine how ANP interferes with Aβ aggregation pathways starting from different aggregated species by ThT (Figure 3a) and (ii) identify which aggregated species (Aβ monomers, oligomers, and fibrils) are more favorable to interact with ANP by SPR (Figure 3e−g). ThT kinetics curves in Figure 3a clearly showed that in all cases, the addition of ANP of different concentrations (5, 10, 20 μM) to different preformed Aβ seeds still induced a strong inhibition effect on Aβ aggregation, as evidenced by the sudden decrease of ThT signals to different extents at the exact points by adding ANP. Specifically, the addition of ANP to 1 h-, 5 h-, and 11 h-Aβ seeds led to an immediate ThT decrease by 102% (red line), 96.1% (blue line), and 77.1% (green line) as compared to pure Aβ aggregation (black line). More impressively, in the case of the co-incubation of ANP with mature Aβ fibrils performed at 24 h, ANP served as "β-sheet breakers" to disaggregate the existing Aβ fibrils in a concentration-dependent manner via a cross-seeding effect. As a result, ANP reduced the amount of Aβ fibrils by 29.1% (light orange line), 42.2% (orange line), and 50.4% (brown line) at molar ratios of ANP/Aβ of 1:2, 1:1, and 2:1, respectively. These seed-induced aggregation of Aβ by ANP clearly indicates that ANP can modify Aβ aggregation pathways differently, depending on Aβ aggregation states, by slowing down the aggregation of small Aβ oligomers or dissembling large Aβ fibrils.

AFM and far-UV CD spectroscopy were also performed to confirm and understand the ANP-induced fibril inhibition and structural transition of different Aβ seeds. As shown in Figure 3c, 20 μM pure Aβ formed a large number of mature fibrils with an average height/length of 33/605 nm (black box), while the co-incubation of 10 μM ANP with 1 h- (red box), 5 h- (blue box), and 11 h- (green box) Aβ seeds led to obvious fibril inhibition and disaggregation, as visualized by a few small spherical aggregates or short fibrils. In the case of ANP-24 h seeded Aβ, the fibril disassembling ability of ANP became more pronounced (orange box), i.e., ANP (10 μM) can bind to multiple sites of Aβ aggregates to disassemble preformed fibrils and convert them into small aggregates. CD spectra also showed that the co-incubation of ANP (10 μM) with different Aβ seeds (i.e., 1, 5, and 11 h) led to the decrease of the characteristic β-sheet-pertaining peak at 195 nm and 215 nm (Figure S3). After 24 h of incubation, the number of β-sheets was reduced by 46.4% (red line), 50.3% (blue line), 32.2% (green line), and 6.7% (orange line) for 1, 5, 11, and 24 h Aβ seeds, respectively (Figures 3b and S3).

From a molecular interaction viewpoint, ANP-induced Aβ inhibition/disaggregation ability mainly stems from their heterotypic interactions with Aβ to competitively block Aβ-Aβ self-interactions, thus preventing and disassembling Aβ fibrillation. To verify this hypothesis, we quantified the binding affinity between ANP and different Aβ seeds using surface plasmon resonance (SPR). Similar to our previously reported SPR studies on the interactions between organic compounds (tabersonine, ginnalin A) and Aβ_{42} and between different heterotypic peptides (4:1-1:0.5, 5:1-0.025),[45,46] ANP monomers were first covalently linked to activated carboxyl groups on carboxymethylated dextran SPR chips via EDC/NHS coupling, followed by the flow of different Aβ seeds solutions (i.e., freshly prepared monomeric Aβ, 11 h-oligomeric Aβ, and 24 h-fibrillar Aβ) to determine if any specific binding occurs between immobilized ANP and Aβ seeds (Figure 3d). At a first glance in Figure 3e−g, ANP-coated surfaces exhibited immediate responses for all Aβ seeds as evidenced by the increase of SPR signals that are dependent on both Aβ concentrations and Aβ seeds. As Aβ concentration increased from 2.5 to 20 μM, its adsorption amount on ANP-coated surfaces increased from 4.9 to 57 ng/cm^2 for Aβ monomers, from 6.8 to 90 ng/cm^2 for Aβ oligomers, and from 2.9 to 107 ng/cm^2 for Aβ fibrils. Meanwhile, the larger Aβ seeds seemed to exhibit higher adsorption amount than the smaller ones on ANP-coated surfaces although these seeds were formed at the

https://doi.org/10.1021/acschemneuro.2c00712
ACS Chem. Neurosci. 2023, 14, 312−322

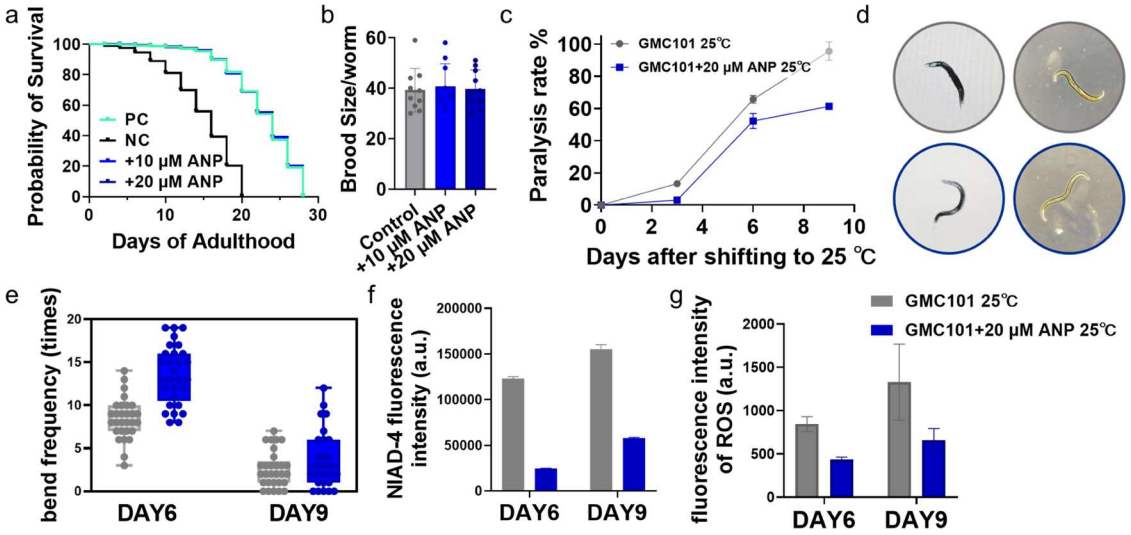

Figure 5. Cross-seeding of ANP with Aβ provides neuroprotection to transgenic *C. elegans* worms. (a) Lifespan and (b) brood size of wild-type (N2) *C. elegans* incubated with and without S-complete buffer (green), 200 nM NaOH (black), 10 μM ANP (blue), and 20 μM ANP (dark blue). Paralysis assays for characterizing the (c) paralysis rate, (d) paralysis state in the liquid medium (1st column), and on agar plates (2nd column), and (e) bend frequency for age-synchronized GMC101 worms treated with or without ANP (20 μM) at 25 °C for 9 days. Fluorescence assays for characterizing (f) Aβ deposition in the head region and (g) intracellular ROS production for age-synchronized GMC101 worms treated with or without ANP (20 μM) at 25 °C for 9 days.

same concentrations. The difference in the adsorption amount is of no statistical significance and does not necessarily correlates with binding affinity, because of the higher molecular weight of the larger Aβ seeds. Evidently, kinetic analysis yielded an equilibrium dissociation constant (K_D) of 1.234 μM for monomeric Aβ, 1.794 μM for oligomeric Aβ, and 1.759 μM for fibrillar Aβ, respectively (Figure S4). These comparable K_D values confirm the general, strong binding of ANP to different Aβ seeds, explaining ANP binding-induced Aβ-inhibition mechanism.

2.3. Cross-Seeding of ANP with Aβ Rescues Amyloid-Mediated Cytotoxicity. It is generally accepted that the aggregation of misfolded Aβ into neurotoxic oligomers and fibrils has been implicated as a key catastrophic event in the pathogenesis of AD. However, due to complex pathological species of Aβ (on-pathway vs off-pathway species), the inhibition of Aβ aggregation does not necessarily inhibit Aβ-induced cytotoxicity. Here, we applied 3-(4,5-dimethylthiazole-2-yl)-2,5-diphenyltetrazolium bromide (MTT) (Figure 4a), lactate dehydrogenase (LDH) (Figure 4b), and live/dead assays (Figure 4c) to study whether the ANP-induced inhibition of Aβ aggregation can also rescue SH-SY5Y neuron cells from Aβ-mediated cytotoxicity. As a control, pure Aβ (20 μM) led to 43% cell viability and 9.6% cell apoptosis upon 24 h of incubation with cells, confirming the high toxicity of Aβ aggregates to the cells. In sharp contrast, pure ANP of different concentrations from 0.1 to 10 μM were almost nontoxic to SH-SY5Y cells (98−108% cell viability and 1.8−2.4% cytotoxicity). When co-incubating ANP with Aβ-treated SH-SY5Y cells, ANP exhibited a dose-dependent cell protection, as indicated by an increase in cell viability by 19−25% and a reduction in cytotoxicity by 20−56% as the ANP concentration increased from 0.1 to 10 μM. Such a protective role of ANP mainly comes from (i) the formation of non- or less-toxic ANP-Aβ hetero-assemblies; (ii) the inhibition of toxic Aβ aggregates; and (iii) the degradation of toxic Aβ aggregates into non- or less-toxic Aβ species, consistent with these ThT and AFM data that Aβ aggregation was largely inhibited and the resultant products were mixtures of few protofibrils and irregular oligomers.

Seeing is understanding, we next performed a live/dead assay to visualize and compare the number of living and dead cells in the presence of Aβ and ANP at a molar ratio of 1:0.5. Calcein AM (green) and ethidium homodimer-1 (red) were used to detect intracellular esterase activity (an indicator for living cells) and nucleic acid with damaged membranes (an indicator for dead cells), respectively. As expected in Figure 4c,d, (i) ANP alone exhibited no toxicity to cells, as observed by the large proportion of live cells (green stains), similar to the uncreated cell group and (ii) the introduction of ANP (10 μM) led to a reduction in dead cells and an increase in living cells simultaneously, again confirming the protection ability of ANP from Aβ-induced cell toxicity. We posit that the strong ANP-Aβ interactions prevent Aβ aggregates from penetrating the cell membrane, thus rescuing the cells from membrane disruption.

2.4. Cross-Seeding of ANP with Aβ Suppresses Aβ-Mediated Dysfunction in Worm Models. To transform this fundamental research into clinically relevant applications, we assessed the neuroprotective effects of ANP on Aβ-induced paralysis, lifespan, brood size, ROS, bending frequency, and plaque formation using wild-type and transgenic *C. elegans*. First, given that a network of transcription factors can modulate the normal aging process, we examined the dose effect of ANP (10−20 μM) on the lifespan and brood size of wild-type *C. elegans*. As shown in Figure 5a,b, serving a supplementary diet of 200 mM NaOH as a negative control caused 100% worm death after 20 days (black line), while 10−20 μM ANP-treated worms (blue line) exhibited a normal survival life cycle of 28 days, as evidenced by the overlapping survival lines between ANP-treated worms (blue line) and untreated worms (green line) (Figure 5a). Next, the brood size assay of worms was performed by counting the number of eggs laid by a single nematode during the first 48 h of adult life. The results showed that the brood size was 40.9 and 39.8 for the worms treated with 10 μM and 20 μM ANP, as compared with

https://doi.org/10.1021/acschemneuro.2c00712
ACS Chem. Neurosci. 2023, 14, 312−322

a brood size of 39.2 for untreated worms, again confirming the nontoxicity of ANP on normal life activities of worms (Figure 5b).

Next, the transgenic *C. elegans* GMC101 strains were used to explore whether ANP could exert a protective effect on the nervous system against Aβ-induced paralysis. GMC101 expresses full-length A$\beta_{1\text{-}42}$ in the body wall muscles and shows an AD-like symptom of the paralysis phenotype caused by Aβ aggregation in the head region upon temperature upshifts from 20 to 25 °C.[47] The experimental concentration of ANP of 20 μM was selected in this paralysis study according to our pre-tests. The worm movement is classified into two distinct states: (i) normal state is defined by free movements of worms without assistance by any external stimuli and (ii) paralyzed state is recognized when the worms do not move or only wave their heads after 3 repeated touches. As shown in Figure 5c, the untreated GMC101 worm showed a typical time-dependent, progressive paralysis, as evidenced by 13.3, 65.7, and 95.7% of paralysis behavior on the 3rd, 6th, and 9th day after temperature shifting, respectively. By comparison, ANP-treated worms showed a decrease in the Aβ-induced paralysis rate by 10.2−34.4% within the same 9 days, suggesting that ANP (20 μM) reduces Aβ-induced paralysis in GMC101.

Seeing is believing, Figure 5d shows microscopy images of GMC101 worms under normal and paralyzed conditions. For example, the untreated worm (gray circle) cultured at 25 °C (i) displayed rigid "rod-like" shape in both liquid medium (1st column) and solid agar plate (2nd column); (ii) showed largely reduced body bending in the liquid medium; and (iii) restricted its movement only to the head region, not the whole body. Differently, the ANP-treated worm (blue circle) exhibited a smooth body shape, normal bending degree, and crawl/swim capacity, indicating 20 μM ANP can effectively suppress in vivo worm paralysis by protecting the worms from Aβ-induced toxicity. Visual inspection also showed that each untreated worm bent ∼8 times on average in 30 seconds on day 6 and ∼2 times on day 9, while each ANP-treated worm bent ∼13 times on day 6 and ∼4 times on day 9 (Figure 5e). To investigate the effect of ANP on Aβ aggregation in GMC101, we used Aβ-specific dye of NIAD-4 to visualize Aβ disposition in the head region of GMC101. Fluorescence images of the head region of the untreated worms incubated at 20 °C (positive control) did not show any Aβ aggregates (red fluorescence, dash line) (Figure S5). Upon temperature shifts to 25 °C, the untreated worms in the negative control showed a significant increase in Aβ deposition. However, the introduction of ANP enabled effective reduction in Aβ deposits (red fluorescence) in worms by 79.8% on day 6 and 62.8% on day 9 (Figure 5f). These results suggest that ANP can inhibit Aβ aggregation and deposition in the muscle cells of transgenic worms.

Oxidative stress is also considered as another contributing factor to AD as it is induced by β-amyloid aggregation. Here, we applied fluorescence probe H_2DCF-DA to measure the intracellular ROS levels, which helps in understanding the antioxidant effect of ANP in vivo. As shown in Figure 5g, the untreated worms exhibited a time-course ROS generation due to the accumulation of Aβ, as indicated by fluorescence intensities of 845 and 1329 au at day 6 and day 9, respectively. However, the worms treated with ANP significantly suppressed the production of ROS to 436 and 658 au on day 6 and day 9, equivalent to 48.4−50.5% reduction from untreated worms. These results indirectly suggest that the delay observed in Aβ-induced paralysis of GMC101 nematodes after treatment with ANP could be attributed to the reduced accumulation of intracellular ROS. Overall, ANP can reduce Aβ aggregates and plaques, attenuate Aβ-induced paralysis, and diminish ROS production caused by oxidative stress, all of which help to retain and prolong the lifespan and health of the worms.

3. CONCLUSIONS

Growing evidence has shown a clinical and pathological connection between CVDs and AD, which mainly focuses on associations between cerebral hypoperfusion and neuronal degradation. Differently, this work aims to provide a new explanation for the link between CVDs and AD by examining the cross-seeding (i.e., heterotypic interactions) between CVD-associated ANP and AD-associated Aβ and understanding the impacts of the cross-seeding on Aβ aggregation and toxicity in vitro and in vivo. Collective aggregation data from ThT, SPR, CD, and AFM confirmed that ANP can cross-seed with different Aβ species (i.e., Aβ monomers, oligomers, and fibrils) with a high binding affinity of 1.234−1.797 μM and exert a dose-dependent inhibition property against Aβ fibrillogenesis via different pathways. The first inhibition pathway of ANP is to prevent the structural transition and elongation of small Aβ monomers and oligomers toward mature Aβ fibrils, leading to almost complete inhibition of Aβ fibrillization and 37% of β-structure reduction at sub-stoichiometric concentrations. The second inhibition pathway of ANP is to disassemble the preformed Aβ fibrils and converted them into small aggregates. In line with ANP-induced inhibition of Aβ aggregation, in vitro cell assays also showed that ANP can protect neuron cells from Aβ-induced cytotoxicity by increasing 25% of cell viability and decreasing 56% of cell toxicity, as compared to those of Aβ-treated cells. Finally, both wild-type and transgenic *C. elegans* worm models showed that ANP (20 μM) can alleviate the AD-like phenotypes of worms from Aβ-induced toxicity, as evidenced by suppressing 34.4% of worm paralysis, improving 100% of worm bending frequency, reducing 79.8% of Aβ plaques in the worm heads, and decreasing 50.5% of ROS production. From a broader viewpoint, compared with other peptide compounds that have shown promise in anti-Aβ fibrillogenesis and ameliorating Aβ-induced cytotoxicity, ANP is unique because it exhibits a more efficient inhibition of Aβ aggregation via different pathways at a lower dosage in vitro and in vivo. This work discovers not only a new cross-seeding system between ANP and Aβ from the two different disease-causative proteins but also a new biological role of ANP in Aβ aggregation, which may reveal a different heart-to-head axis for the onset and progression of a neurodegenerative process.

4. EXPERIMENTAL PROCEDURES

4.1. Reagents. Amyloid β (Aβ_{1-42}, ≥95%) and atrial natriuretic peptide (ANP, ≥95%) were purchased from CPC Scientific (Sunnyvale, CA). 1,1,1,3,3,3-Hexafluoro-2-propanol (HFIP, ≥99.9%), dimethyl sulfoxide (DMSO, ≥99.9%), and thioflavin T (ThT, 98%) were commercially available from Sigma Aldrich (St. Louis, MO). All other chemicals were of the highest grade available.

4.2. Peptide Purification and Preparation. All of the peptides were stored at −20 °C once received. All prepackaged peptides (i.e., Aβ and ANP) were redissolved in HFIP at 1 mg/mL concentration and incubated at ambient temperature for 2 h, followed by 30 min sonication in an ice bath and high-speed centrifugation at 14,000 rpm at 4 °C to further break potential Aβ aggregates. Finally, the only top 80% of the supernate was extracted and used as Aβ_{42} monomer

https://doi.org/10.1021/acschemneuro.2c00712
ACS Chem. Neurosci. 2023, 14, 312−322

solution. The peptides were sub-packaged and stored at −80 °C before use. Unless otherwise states, all peptides were pre-solubilized in DMSO, then further dissolve in different buffers to reach the desired concentration.

4.3. Thioflavin T (ThT) Fluorescence Assay. Amyloidosis kinetics of Aβ was monitored using a SpectraMax M3 microplate reader (Molecular Devices, CA) and measured at an excitation wavelength of 450 nm and emission wavelength in a range of 470−500 nm under a kinetic top-read mode. To determine the effect of ANP on monomeric Aβ, samples were prepared on ice by mixing Aβ-DMSO (DMSO% = 5%) with ANP in different molar ratios (1:0.005−1:0.5) to achieve a final test volume of 200 μL. After transferring the samples to a 96-well plate in the plate reader, 1 μL of 2 mM ThT was quickly added to each well before the aggregation was initiated at 37 °C, then fluorescence intensity data were recorded consistently at 30 min intervals for 24 h. For the seeding experiment, 5 μL of the ANP-DMSO mixture was added to aggregating Aβ solution at 1, 5, 11, and 24 h, and aggregation curves were monitored to illustrate cross-seeding between ANP and seeded Aβ.

4.4. Circular Dichroism Spectroscopy (CD). The secondary structure of the protein was monitored by far-UV CD spectroscopy with a J-1500 spectropolarimeter (Jasco Inc., Japan) under the continuous scanning mode at room temperature. In all, 20 μM Aβ were incubated at 37 °C in 10 mM phosphate-buffered saline (PBS, pH 7.4) in the presence or absence of 1/10 μM ANP; 150 mL of samples were pipetted into a 1 mm optical path length CD cuvette and the spectra were scanned between 190 and 250 nm with a step size of 0.5 nm and 50 nm/min scan rate, in all CD measurements after each time interval. All received spectra were analyzed by subtracting the PBS buffer baseline to remove background influence. The secondary structural contents were determined using the β Structure Selection (BeStSel) algorithm[48] (http://bestsel.elte.hu/).

4.5. Atomic Force Microscopy (AFM). The morphology changes of amyloid peptides during aggregation were imaged using a Nanoscope III multimode AFM (Veeco, NY). At different time intervals, 20 μL of the samples were deposited on a freshly cleaved mica sheet for 5 min at ambient temperature. The sample was then washed three times using Mill-Q water to remove salts and dried with air gas before being stored in sealed containers. The cantilever resonance frequency was 45−95 kHz. The images (256 pixels × 256 pixels) were captured using a scan size of 3 μm. Representative AFM images were obtained by scanning six different locations on the mica surface.

4.6. Surface Plasmon Resonance (SPR) Spectroscopy. The binding analysis was performed using a custom-built four-channel SPR instrument at ambient temperature. A dextran-modified SPR sensor chip was prepared following the well-established method.[49] Briefly, the clean gold surface was first immersed in 5 mM 11-mercapto-1-undecanol in ethanol/water (8:2) solution for 24 h to obtain the thiol-based surface, followed by reacting with epichlorohydrin (2% v/v) in 0.1 M NaOH for 3 h and transferred to a 300 g/L dextran solution (500 kDa) in 0.1 M NaOH for 24 h to obtain carboxymethylated dextran-modified SPR chips. The resultant surfaces were finally washed with Milli-Q water and subsequently immersed in 1.0 M bromoacetic acid in 2 M NaOH for 24 h to achieve the dextran-modified SPR sensor chip.

For ANP immobilization, the SPR chips were first activated with an equimolar mixture of *N*-hydroxysuccinimide (NHS) and *N*-ethyl-*N*-(diethylaminopropyl)carbodiimide (EDC). Subsequently, ANP dissolved in PBS (10 mM, pH = 7.4) was introduced to the sample surface for 10 min, and the remaining NHS-ester groups were blocked by flowing 1 M ethanolamine HCl (pH = 8.5) for another 10 min. The binding affinity of defensins with amyloid peptides was determined by injecting a serially diluted Aβ (2.5−20 μM) in running buffer (10 mM PBS, pH = 7.4) over channels at a flow rate of 5 μL/min, followed by PBS buffer to remove any unbound amyloid peptides. Dissociation constant (K_D) values were evaluated using Anabel software (http://anabel.skscience.org/) by fitting the data using a 1:1 Langmuir binding model and observed by the binding constant (k_{obs}) linearization method.

4.7. Cell Culture. Neuroblastoma cell line SH-SY5Y (ATCC CRL-2266, Manassas, VA) was selected to investigate the protection ability of ANP on Aβ-induced cytotoxicity. SH-SY5Y cell lines were cultured in DMEM (Sigma Aldrich, St. Louis, MO) supplemented with 10% (v/v) fetal bovine serum (VWR, Radnor, PA) and 1% (v/v) penicillin/streptomycin (Sigma Aldrich, St. Louis, MO) in a T25 flask in humidified air containing 5% CO_2 at 37 °C. After cells reach ∼80% confluence, they were then harvested using 0.25 mg/mL Trypsin/EDTA solution (Sigma Aldrich, St. Louis, MO) and seeded in a 96-well plate (2×10^4 per well).

4.8. MTT Reduction Assay. Cellular metabolic activity as an indicator of cell viability was determined by the well-established 3-(4,5-dimethylthiazole-2-yl)-2,5-diphenyltetrazolium bromide (MTT) reduction assay. The cell-seeded 96-well plates were incubated for 24 h to allow them to attach. Then replaced with fresh cell culture medium with Aβ/ANP/Aβ-ANP solutions and cultured for another 24 h at 37 °C and 5% CO_2 in a humidified incubator. After 24 h, the cells were labeled in 0.5 mg/mL MTT culture medium solution at 37 °C for 4 h and dissolved formazan crystals in dimethyl sulfoxide. The absorbance value was read at 540 nm using a SpectraMax M3 microplate reader, and the cell viability was determined as the percentage of MTT reduction as compared to untreated cells. Each sample was counted in triplicate and reported as mean ± SD.

4.9. LDH Cytotoxicity Assay. The cytotoxicity of amyloid peptides was assessed by lactate dehydrogenase (LDH) activity. Soluble enzyme LDH found in the cytoplasm would be released into the cell medium and therefore act as an indicator of irreversible cell death due to cell membrane damage.[50] LDH assay was performed using a CytoSelect LDH Cytotoxicity Assay Kit (Cell Biolabs, San Diego). In short, spontaneous LDH release was measured as a positive control in untreated cells, and the total LDH release was measured by cell lysis as a negative control in Triton X-100 solution. The plates were then incubated for 10 min at room temperature, followed by transferring 90 μL of medium from each well to a clean 96-well plate. The leaked LDH activity in the medium was evaluated by adding 10 μL of LDH cytotoxicity assay reagent and incubated for 30 min, and the absorbance was read at a wavelength of 450 nm using a microplate reader. The LDH activity values were normalized to spontaneous LDH release, and cytotoxicity values were calculated in percentages of total LDH release. Each sample was counted in triplicate and reported as mean ± SD.

4.10. LIVE/DEAD Viability/Cytotoxicity Assay. The representative images of the live and dead cells were acquired to evaluate the protection effects of ANP on Aβ-induced cytotoxicity. SH-SY5Y cells incubated with or without Aβ/ANP/Aβ-ANP were stained using a LIVE/DEAD Viability/Cytotoxicity Kit (L3224, Invitrogen) and imaged using a fluorescence microscope (Echo RVL2-K) to visualize the live and dead cells. Corresponding fluorescence intensity was calculated using ImageJ (n = 3).

4.11. Maintenance of *C.elegans*. *C. elegans* strains used in this study (i) dvIs100[unc-54p::A-β-1-42::unc543′UTR + mtl-2p::GFP] (GMC101) and (ii) wild-type (N2) were provided by the Caenorhabditis Genetics Center (University of Minnesota). *C. elegans* strains were moved to a nematode growth medium (NGM) agar plate seeded with *Escherichia coli* strain (OP50) and incubated at 20 °C unless stated otherwise. To obtain the synchronous population, gravid adults were collected and centrifuged. Then, 5 mL of bleach solution (2.75 mL of Mill-Q water, 1.25 mL of 1 M NaOH, and 1 mL of bleach) was added to the worm pellet until all of the adults broke out, followed by washing and hatching overnight in S-complete buffer. The hatched worms were counted and the concentration was determined before use. After reaching the L4 larval stage, 5-fluoro-2′-deoxyuridine (FudR) was added to inhibit the growth of offspring.

4.12. Wild-type *C.elegans* Lifespan Assay. Lifespan assay was modified slightly according to the methods described previously.[51] Briefly, age-synchronized worms were transferred to a 96-well plate and each well contain ∼10 worms, a total of 15 wells were used for each treatment group. The plate was sealed to avoid contamination and evaporation and the worms were allowed to grow up to the L4 stage, followed by the addition of 30 μL of 0.6 mM FUDR stock

https://doi.org/10.1021/acschemneuro.2c00712
ACS Chem. Neurosci. 2023, 14, 312−322

solution to each well. Then, 5 μL of ANP solution prepared in S-complete buffer containing <0.1% DMSO at an appropriate concentration (10 μM/20 μM) was added to each well. As positive and negative controls, the same amount of S-complete buffer-DMSO or 1 M NaOH was added to each well, respectively. After adding drugs, the number of surviving worms was counted under a microscope at two-day intervals until all of the worms were dead.

4.13. Wild-type *C.elegans* Brood Size Assay. A total of 30 age-synchronized gravid adult worms were randomly assigned to nontreated, 10 μM ANP-treated, and 20 μM ANP treatment NGM wells with a concentration of 1 worm/well. After 24 h, the number of hatched worms was counted for each well.

4.14. Transgenic *C.elegans* Paralysis Assay. Age-synchronized worms were grown at 20 °C until the L4 larval stage and then transferred to fresh 3.5 cm NGM agar plates treated with control-DMSO plates or ANP. For each treatment group, a total of six individual plates were tested, and each plate contained ∼30 worms. Plates were immediately shifted to 25 °C and paralysis was scored every 1 day after the temperature shift.

On days 6 and 9, worms were scored as paralyzed if they failed to move during observation and failed to respond to touch-provoked movements with a platinum wire. Representative worms were transferred to liquid M9 buffer or agar for further imaging. Then, 1 mL M9 buffer was added to one of the plates of worms, followed by counting the bending frequency in 30 s.

4.15. Staining and Microscopy in Transgenic *C. elegans*. Ten worms were randomly selected from day 6 and day 9 and different treatment plates and incubated with 1 μM NIAD-4 (0.1% DMSO in M9 buffer) for 4 h at room temperature exhibiting robust and reproducible staining. Worms/NIAD solution was then transferred on 2% agarose pads containing 40 mM NaN3 as an anesthetic on glass microscope slides for imaging. Images were captured using a fluorescence microscope (Olympus IX81) with a 40× objective and a CY3/DAPI filter. Fluorescence intensity was calculated using ImageJ software and normalized as the corrected total cell fluorescence. Only the head region was considered because of the high background signal in the guts.

4.16. Transgenic *C.elegans* ROS Assay. A hundred worms were collected in a tube with 500 μL of M9 containing 50 μM H2DCF-DA, followed by incubation for 2 h in the dark with vortex. Then, the worms were washed 2 times with M9 buffer and transferred to a 96-well plate with a concentration of 20 worms/well. A SpectraMax M3 microplate reader (Molecular Devices, CA) was used to measure the fluorescence intensity at an excitation wavelength of 485 nm and an emission wavelength of 530 nm under top-read mode.

■ ASSOCIATED CONTENT

Supporting Information

The Supporting Information is available free of charge at https://pubs.acs.org/doi/10.1021/acschemneuro.2c00712.

AFM images, CD spectra, and corresponding secondary structure content, dissociation constant analysis, NIAD-4 staining in worm's body, and comparison of different peptide-based Aβ inhibitors (PDF)

■ AUTHOR INFORMATION

Corresponding Author

Jie Zheng − *Department of Chemical, Biomolecular, and Corrosion Engineering, The University of Akron, Akron, Ohio 44325, United States;* orcid.org/0000-0003-1547-3612; Email: zhengj@uakron.edu

Authors

Yijing Tang − *Department of Chemical, Biomolecular, and Corrosion Engineering, The University of Akron, Akron, Ohio 44325, United States*

Dong Zhang − *Department of Chemical, Biomolecular, and Corrosion Engineering, The University of Akron, Akron, Ohio 44325, United States;* orcid.org/0000-0001-7002-7661

Yung Chang − *R&D Center for Membrane Technology and Department of Chemical Engineering, Chung Yuan Christian University, Taoyuan 32023, Taiwan;* orcid.org/0000-0003-1419-4478

Complete contact information is available at: https://pubs.acs.org/10.1021/acschemneuro.2c00712

Author Contributions

Y.T. and J.Z., initiated the idea of this project. Y.T., D.Z., and Y.Z. designed and conducted experiments in vitro. Y.L., Y.M., K.G. designed and conducted molecular simulations. J.Z. supervised this project. The manuscript was written through inputs from all authors. All authors have given approval to the final version of the manuscript.

Notes

The authors declare no competing financial interest.

The data that support the findings of this study are available from the corresponding author and co-authors upon reasonable request. All relevant data for the figures are included in the Supporting Information files. Source data has been provided as Supplementary Data.

All data are available in the main text or the supplementary materials.

■ ACKNOWLEDGMENTS

We thank financial support from NSF-CBET-2107619 and the Faculty Summer Research Fellowship from The University of Akron. We also trained three K12 students of Bowen Zheng from Copley High School, Alice Xu from Hudson High School, and Keven Gong from Hudson Middle School via this project.

■ REFERENCES

(1) Karran, E.; Mercken, M.; Strooper, B. D. The amyloid cascade hypothesis for Alzheimer's disease: an appraisal for the development of therapeutics. *Nat. Rev. Drug Discovery* **2011**, *10*, 698.

(2) Bolognesi, M. L.; Gandini, A.; Prati, F.; Uliassi, E. From Companion Diagnostics to Theranostics: A New Avenue for Alzheimer's Disease? *J. Med. Chem.* **2016**, *59*, 7759.

(3) Breijyeh, Z.; Karaman, R. Comprehensive review on Alzheimer's disease: Causes and treatment. *Molecules* **2020**, *25*, 5789.

(4) Zhang, F.; Niu, L.; Li, S.; Le, W. Pathological Impacts of Chronic Hypoxia on Alzheimer's Disease. *ACS Chem. Neurosci.* **2019**, *10*, 902.

(5) Sun, Y.-Y.; Wang, Z.; Zhou, H.-Y.; Huang, H.-C. Sleep−Wake Disorders in Alzheimer's Disease: A Review. *ACS Chem. Neurosci.* **2022**, *13*, 1467.

(6) Zhang, M.; Zhao, D.; Zhou, G.; Li, C. Dietary Pattern, Gut Microbiota, and Alzheimer's Disease. *J. Agric. Food. Chem.* **2020**, *68*, 12800.

(7) Yang, J.; Li, S.; He, X.-B.; Cheng, C.; Le, W. Induced pluripotent stem cells in Alzheimer's disease: applications for disease modeling and cell-replacement therapy. *Mol. Neurodegener.* **2016**, *11*, 39.

(8) Masters, C. L.; Bateman, R.; Blennow, K.; Rowe, C. C.; Sperling, R. A.; Cummings, J. L. Alzheimer's disease. *Nat. Rev. Dis. Primers* **2015**, *1*, 15056.

(9) Snyder, H. M.; Corriveau, R. A.; Craft, S.; Faber, J. E.; Greenberg, S. M.; Knopman, D.; Lamb, B. T.; Montine, T. J.; Nedergaard, M.; Schaffer, C. B.; et al. Vascular contributions to cognitive impairment and dementia including Alzheimer's disease. *Alzheimer's Dement.* **2015**, *11*, 710.

(10) Santiago, J. A.; Potashkin, J. A. The impact of disease comorbidities in Alzheimer's disease. *Front. Aging Neurosci.* **2021**, *13*, 38.
(11) Kalaria, R. N. The role of cerebral ischemia in Alzheimer's disease. *Neurobiol. Aging* **2000**, *21*, 321.
(12) Bogers, R. P.; Bemelmans, W. J.; Hoogenveen, R. T.; Boshuizen, H. C.; Woodward, M.; Knekt, P.; Van Dam, R. M.; Hu, F. B.; Visscher, T. L.; Menotti, A. Association of overweight with increased risk of coronary heart disease partly independent of blood pressure and cholesterol levels: a meta-analysis of 21 cohort studies including more than 300 000 persons. *Arch. Intern. Med.* **2007**, *167*, 1720.
(13) El Gaamouch, F.; Jing, P.; Xia, J.; Cai, D. Alzheimer's disease risk genes and lipid regulators. *J. Alzheimer's Dis.* **2016**, *53*, 15.
(14) Van Cauwenberghe, C.; Van Broeckhoven, C.; Sleegers, K. The genetic landscape of Alzheimer disease: clinical implications and perspectives. *Genet. Med.* **2016**, *18*, 421.
(15) Iadecola, C.; Davisson, R. L. Hypertension and cerebrovascular dysfunction. *Cell Metab.* **2008**, *7*, 476.
(16) de la Torre, J. C. How do heart disease and stroke become risk factors for Alzheimer's disease? *Neurol. Res.* **2006**, *28*, 637.
(17) Willis, M. S.; Patterson, C. Proteotoxicity and cardiac dysfunction—Alzheimer's disease of the heart? *N. Engl. J. Med.* **2013**, *368*, 455.
(18) Tini, G.; Scagliola, R.; Monacelli, F.; La Malfa, G.; Porto, I.; Brunelli, C.; Rosa, G. M. Alzheimer's disease and cardiovascular disease: a particular association. *Cardiol. Res. Pract.* **2020**, *2020*, No. 2617970.
(19) Rosendorff, C.; Beeri, M. S.; Silverman, J. M. Cardiovascular risk factors for Alzheimer's disease. *Am. J. Geriatr. Cardiol.* **2007**, *16*, 143.
(20) Watts, A.; Crimmins, E. M.; Gatz, M. Inflammation as a potential mediator for the association between periodontal disease and Alzheimer's disease. *Neuropsychiatr. Dis. Treat.* **2008**, *4*, 865.
(21) Peers, C.; Dallas, M. L.; Boycott, H. E.; Scragg, J. L.; Pearson, H. A.; Boyle, J. P. Hypoxia and neurodegeneration. *Ann. N. Y. Acad. Sci.* **2009**, *1177*, 169.
(22) Stakos, D. A.; Stamatelopoulos, K.; Bampatsias, D.; Sachse, M.; Zormpas, E.; Vlachogiannis, N. I.; Tual-Chalot, S.; Stellos, K. The Alzheimer's disease amyloid-beta hypothesis in cardiovascular aging and disease: JACC focus seminar. *J. Am. Coll. Cardiol.* **2020**, *75*, 952.
(23) Murphy, J.; Van Le, T. N.; Fedorova, J.; Yang, Y.; Krause-Hauch, M.; Davitt, K.; Zoungrana, L. I.; Fatmi, M. K.; Lesnefsky, E. J.; Li, J.; Ren, D. The Cardiac Dysfunction Caused by Metabolic Alterations in Alzheimer's Disease. *Front. Cardiovasc. Med.* **2022**, *9*, No. 850538.
(24) Leszek, J.; Mikhaylenko, E. V.; Belousov, D. M.; Koutsouraki, E.; Szczechowiak, K.; Kobusiak-Prokopowicz, M.; Mysiak, A.; Diniz, B. S.; Somasundaram, S. G.; Kirkland, C. E. The Links between Cardiovascular Diseases and Alzheimer's Disease. *Curr. Neuropharmacol.* **2021**, *19*, 152.
(25) Nag, N.; Tripathi, T. Cross-Seeding with Homologous Sequences Alters Amyloid Aggregation Kinetics and Fibril Structure. *ACS Chem. Neurosci.* **2022**, *13*, 537.
(26) Konstantoulea, K.; Guerreiro, P.; Ramakers, M.; Louros, N.; Aubrey, L. D.; Houben, B.; Michiels, E.; De Vleeschouwer, M.; Lampi, Y.; Ribeiro, L. F.; et al. Heterotypic Amyloid β interactions facilitate amyloid assembly and modify amyloid structure. *EMBO J.* **2022**, *41*, No. e108591.
(27) Burnett, J. C., Jr; Kao, P.; Hu, D.; Heser, D.; Heublein, D.; Granger, J.; Opgenorth, T.; Reeder, G. Atrial natriuretic peptide elevation in congestive heart failure in the human. *Science* **1986**, *231*, 1145.
(28) Rao, S.; Pena, C.; Shurmur, S.; Nugent, K. Atrial natriuretic peptide: structure, function, and physiological effects: a narrative review. *Curr. Cardiol. Rev.* **2021**, *17*, 17−27.
(29) Johansson, B.; Wernstedt, C.; Westermark, P. Atrial natriuretic peptide deposited as atrial amyloid fibrils. *Biochem. Biophys. Res. Commun.* **1987**, *148*, 1087.
(30) Yang, Z.; Subati, T.; Kim, K.; Murphy, M. B.; Dougherty, O. P.; Christopher, I. L.; Van Amburg, J. C.; Woodall, K. K.; Barnett, J. V.; Murray, K. T. Natriuretic Peptide Oligomers Cause Proarrhythmic Metabolic and Electrophysiological Effects in Atrial Myocytes. *Circulation* **2022**, *15*, No. e010636.
(31) Wang, Q.; Liang, G.; Zhang, M.; Zhao, J.; Patel, K.; Yu, X.; Zhao, C.; Ding, B.; Zhang, G.; Zhou, F.; Zheng, J. De novo design of self-assembled hexapeptides as β-amyloid (Aβ) peptide inhibitors. *ACS Chem. Neurosci.* **2014**, *5*, 972.
(32) Kholova, I.; Niessen, H. Amyloid in the cardiovascular system: a review. *J. Clin. Pathol.* **2005**, *58*, 125.
(33) Kaye, G. C.; Butler, M.; d'Ardenne, A.; Edmondson, S.; Camm, A.; Slavin, G. Isolated atrial amyloid contains atrial natriuretic peptide: a report of six cases. *Heart* **1986**, *56*, 317.
(34) Boche, D.; Zotova, E.; Weller, R.; Love, S.; Neal, J. W.; Pickering, R.; Wilkinson, D.; Holmes, C.; Nicoll, J. Consequence of Aβ immunization on the vasculature of human Alzheimer's disease brain. *Brain* **2008**, *131*, 3299.
(35) Wong, K. M.; Robang, A. S.; Lint, A. H.; Wang, Y.; Dong, X.; Xiao, X.; Seroski, D. T.; Liu, R.; Shao, Q.; Hudalla, G. A.; et al. Engineering β-Sheet Peptide Coassemblies for Biomaterial Applications. *J. Phys. Chem. B* **2021**, *125*, No. 13599.
(36) Goyal, D.; Shuaib, S.; Mann, S.; Goyal, B. Rationally designed peptides and peptidomimetics as inhibitors of amyloid-β (Aβ) aggregation: potential therapeutics of Alzheimer's disease. *ACS Comb. Sci.* **2017**, *19*, 55.
(37) Anand, B. G.; Prajapati, K. P.; Purohit, S.; Ansari, M.; Panigrahi, A.; Kaushik, B.; Behera, R. K.; Kar, K. Evidence of Anti-amyloid Characteristics of Plumbagin via Inhibition of Protein Aggregation and Disassembly of Protein Fibrils. *Biomacromolecules* **2021**, *22*, 3692.
(38) Zhang, Y.; Tang, Y.; Liu, Y.; Zhang, D.; Zheng, J. Design and Engineering of Amyloid Aggregation-Prone Fragments and Their Antimicrobial Conjugates with Multi-Target Functionality. *Adv. Funct. Mater.* **2021**, *31*, No. 2102978.
(39) Ren, B.; Tang, Y.; Zhang, D.; Liu, Y.; Zhang, Y.; Chen, H.; Hu, R.; Zhang, M.; Zheng, J. Conformational-specific self-assembled peptides as dual-mode, multi-target inhibitors and detectors for different amyloid proteins. *J. Mater. Chem. B* **2022**, *10*, 1754.
(40) Cruz, M.; Tusell, J.; Grillo-Bosch, D.; Albericio, F.; Serratosa, J.; Rabanal, F.; Giralt, E. Inhibition of β-amyloid toxicity by short peptides containing N-methyl amino acids. *J. Pept. Res.* **2004**, *63*, 324.
(41) Liu, J.; Wang, W.; Zhang, Q.; Zhang, S.; Yuan, Z. Study on the efficiency and interaction mechanism of a decapeptide inhibitor of β-amyloid aggregation. *Biomacromolecules* **2014**, *15*, 931.
(42) Taylor, M.; Moore, S.; Mayes, J.; Parkin, E.; Beeg, M.; Canovi, M.; Gobbi, M.; Mann, D. M.; Allsop, D. Development of a proteolytically stable retro-inverso peptide inhibitor of β-amyloid oligomerization as a potential novel treatment for Alzheimer's disease. *Biochemistry* **2010**, *49*, 3261.
(43) Zhang, Y.; Liu, Y.; Tang, Y.; Zhang, D.; He, H.; Wu, J.; Zheng, J. Antimicrobial α-defensins as multi-target inhibitors against amyloid formation and microbial infection. *Chem. Sci.* **2021**, *12*, 9124.
(44) Tang, Y.; Zhang, D.; Zhang, Y.; Liu, Y.; Miller, Y.; Gong, K.; Zheng, J. Cross-seeding between Aβ and SEVI indicates a pathogenic link and gender difference between alzheimer diseases and AIDS. *Commun. Biol.* **2022**, *5*, 1.
(45) Kai, T.; Zhang, L.; Wang, X.; Jing, A.; Zhao, B.; Yu, X.; Zheng, J.; Zhou, F. Tabersonine inhibits amyloid fibril formation and cytotoxicity of Aβ (1−42). *ACS Chem. Neurosci.* **2015**, *6*, 879.
(46) Fan, Q.; Liu, Y.; Wang, X.; Zhang, Z.; Fu, Y.; Liu, L.; Wang, P.; Ma, H.; Ma, H.; Seeram, N. P.; et al. Ginnalin A inhibits aggregation, reverses fibrillogenesis, and alleviates cytotoxicity of amyloid β (1−42). *ACS Chem. Neurosci.* **2020**, *11*, 638.
(47) Kalmankar, N. V.; Hari, H.; Sowdhamini, R.; Venkatesan, R. Disulfide-Rich Cyclic Peptides from Clitoria ternatea Protect against β-Amyloid Toxicity and Oxidative Stress in Transgenic *Caenorhabditis elegans*. *J. Med. Chem.* **2021**, *64*, 7422.
(48) Micsonai, A.; Wien, F.; Kernya, L.; Lee, Y.-H.; Goto, Y.; Réfrégiers, M.; Kardos, J. Accurate secondary structure prediction and

fold recognition for circular dichroism spectroscopy. *Proc. Natl. Acad. Sci.* **2015**, *112*, No. E3095.
(49) Li, Z.; Narouz, M. R.; Munro, K.; Hao, B.; Crudden, C. M.; Horton, J. H.; Hao, H. Carboxymethylated dextran-modified n-heterocyclic carbene self-assembled monolayers on gold for use in surface plasmon resonance biosensing. *ACS Appl. Mater. Interfaces* **2017**, *9*, 39223.
(50) Fotakis, G.; Timbrell, J. A. In vitro cytotoxicity assays: comparison of LDH, neutral red, MTT and protein assay in hepatoma cell lines following exposure to cadmium chloride. *Toxicol. Lett.* **2006**, *160*, 171.
(51) Solis, G. M.; Petrascheck, M. Measuring *Caenorhabditis elegans* life span in 96 well microtiter plates. *J. Visualized Exp.* **2011**, No. e2496.

https://doi.org/10.1021/acschemneuro.2c00712
ACS Chem. Neurosci. 2023, 14, 312−322